

## Fast and wide-range optical beam steering with ultralow side lobes by applying an optimized multi-circular optical phased array

FANGZHENG ZHANG,<sup>1,\*</sup>  DAOCHENG ZHANG,<sup>1</sup> AND SHILONG PAN<sup>1,2</sup> 

<sup>1</sup>College of Electronic and Information Engineering, Nanjing University of Aeronautics and Astronautics, Nanjing 210016, China

<sup>2</sup>e-mail: pans@nuaa.edu.cn

\*Corresponding author: zhangfangzheng@nuaa.edu.cn

Received 14 March 2018; revised 11 May 2018; accepted 15 May 2018; posted 16 May 2018 (Doc. ID 326115); published 12 June 2018

A multi-circular optical phased array (OPA) is proposed and investigated through simulation to realize fast and wide-range optical beam steering with ultralow side lobes. The proposed multi-circular OPA has a circularly symmetrical distribution, and its radical element spacings are optimized by a modified genetic algorithm to achieve the best side lobe suppression. Specifically, the peak side lobe level (PSLL) of the far-field pattern in 0° beam direction reaches as low as 0.0715 for a 73-element optimized multi-circular OPA, which is much better than a multi-circular OPA with uniform radical element spacing (the PSLL is 0.3686). The prominent feature of the proposed OPA is that, once the OPA is optimized towards a specific elevation direction by the modified genetic algorithm, a wide-angle optical beam steering with nearly the same side lobe suppression can be achieved without updating the OPA distribution, which makes it possible for fast optical beam steering over a wide scanning range. In the simulation, ultralow side lobe beam steering with an elevation angle from 0° to 30° and an azimuth angle from 0° to 360° is achieved with the PSLL variation less than 0.001. The relationship between the optimized PSLL and the elevation angle used for OPA optimization is also investigated, which is helpful in achieving the best side lobe suppression for different scanning ranges. The proposed OPA is expected to find applications such as laser radar, high-resolution display, and free space optical communications. © 2018 Optical Society of America

**OCIS codes:** (280.5110) Phased-array radar; (050.1940) Diffraction; (200.2605) Free-space optical communication.

<https://doi.org/10.1364/AO.57.004977>

### 1. INTRODUCTION

Optical beam steering plays an important role in laser radar, free space optical communication, imaging, high-resolution display, etc. [1–6]. Optical phased array (OPA) is a promising beam steering method, which can implement agile beam steering without moving or rotating the facilities. Advantages of applying OPAs for optical beam steering include low cost, chip scale, lightweight, high resolution, random-access pointing, programmable multiple simultaneous beams, and a dynamic focus/defocus capability. The major drawback of a typical uniform OPA is the limited beam scanning range due to the existence of grating lobes in the far-field pattern. Considering the state-of-the-art fabrication level [2,3,7–10], the minimum interelement spacing of an OPA is much larger than half of the light wavelength, which leads to the formation of many grating lobes in the far field. To achieve a wide-range optical beam steering applying an OPA, it is highly required to eliminate or reduce the effect of the grating lobes. To achieve this goal, a few methods have been proposed. Among these methods, an OPA with density tapering (or unequally spaced OPA) is an

effective approach to suppress the grating lobes, which has been extensively investigated in recent years [11–13]. By applying density tapering, the grating lobes of a uniform OPA can be suppressed, and their power is partially transferred to other undesired components called side lobes, which can be further suppressed by optimizing the element distribution of the OPA. The previously reported OPAs with density tapering have mainly adopted two-dimensional rectangular arrays. Although the side lobes can be well suppressed for a specific beam direction after optimization of the element distribution [14], the side lobe level may rise dramatically once the desired beam direction changes. This is caused by the circularly asymmetric structure of a rectangular OPA. Thus, to implement wide-angle optical beam steering, the element spacing of the rectangular OPA should be continually updated to ensure the side lobes are well suppressed. This would inevitably increase the system complexity and limit the beam steering speed.

In this paper, we propose and numerically investigate, to the best of our knowledge, a novel multi-circular OPA to implement fast and valid wide-range optical beam steering, which

can provide a design and optimization model for state-of-the-art OPA configurations [2,3,7–10]. To achieve the best side lobe suppression, a modified genetic algorithm is adopted to optimize the OPA distribution. Besides the great side lobe suppression capability, another advantage of the optimized circular OPA is that optical beam steering in a wide two-dimensional scanning range can be achieved without reconfiguring the OPA element distribution, and a nearly constant peak side lobe level (PSLL) can be achieved within the whole beam steering range. Therefore, a simplified and fast optical beam steering with a large scanning range can be realized. In this study, performance of the proposed OPA is investigated and analyzed through extensive numerical simulations. The relationship between PSLL and scanning ranges are also investigated under different fabrication conditions.

## 2. PRINCIPLE

Figure 1 shows the structure of the proposed multi-circular OPA, which consists of  $M$  rings with  $N$  phase elements distributed equally in each ring, and a phase element located at the center. The total number of elements is  $M \times N + 1$ . In Fig. 1,  $D_m$  denotes the radius of the  $m$ th ring, and  $\sigma_m$  denotes the distance between two adjacent elements in the  $m$ th concentric ring array ( $1 \leq m \leq M$ ). The radiating elements of the circular OPA are assumed to be isotropic point radiators and placed on the  $x$ - $y$  plane. Position of the  $n$ th array element ( $1 \leq n \leq N$ ) located on the  $m$ th concentric ring array is denoted by  $(m, n)$ . In this case, the far-field pattern radiated in the observation is calculated to be [15]

$$E(r, \theta, \phi) = \sum_{m=1}^M \sum_{n=1}^N \omega_{mn} \frac{e^{-jkR_{mn}}}{R_{mn}}, \quad (1)$$

where  $\omega_{mn}$  denotes the excitation coefficient (with amplitude and phase) of the element at  $(m, n)$ ,  $R_{mn}$  is the distance between the element and the observation point,  $(\theta, \phi)$  is the far-field

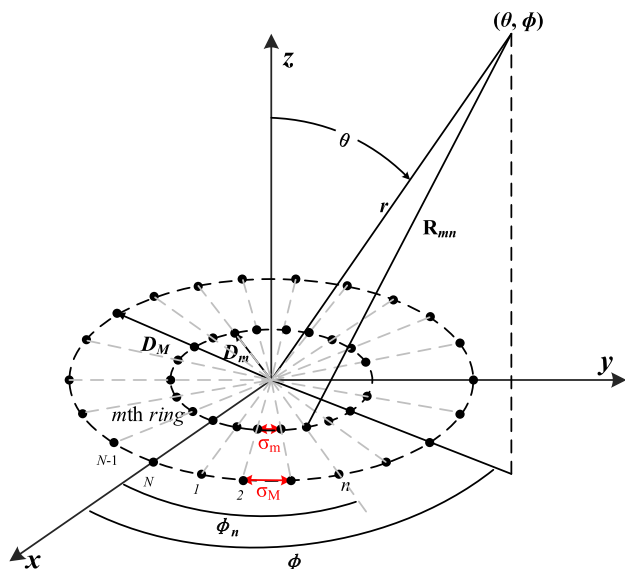


**Fig. 1.** Geometry of the multi-circular OPA with  $M \times N + 1$  element.

position in a spherical coordinate, and  $k = 2\pi/\lambda$  ( $\lambda$  is the light wavelength) is the wave vector. In this paper, we consider the OPAs with uniform amplitude excitation, i.e.,  $|\omega_{mn}| = 1$ . To realize beam steering in the direction  $(\theta_s, \phi_s)$ , the phase excitation  $\alpha_{mn}$  of element  $(m, n)$  should be chosen as

$$\alpha_{mn} = -kD_m \sin \theta_s \cos(\phi_s - \phi_n). \quad (2)$$

In the far-field region,  $r \gg D_M$  is satisfied, and  $R_{mn}$  can be written as

$$R_{mn} = r - D_m \sin \theta \cos(\phi - \phi_n), \quad (3)$$

where  $r$  is the distance between the central element and the observation point, and  $\phi_n = 2n\pi/N$  denotes the angular position of the element at  $(m, n)$ . For far-field observation,  $R_{mn} \approx r$  is satisfied, and the far-field pattern in Eq. (1) can be rewritten as

$$E(r, \theta, \phi) = \frac{e^{-jkr}}{r} [\text{AF}(\theta, \phi)], \quad (4)$$

where the array factor  $\text{AF}(\theta, \phi)$  is expressed as

$$\text{AF}(\theta, \phi) = 1 + \sum_{m=1}^M \sum_{n=1}^N e^{jkD_m \sin \theta \cos(\phi - \phi_n) + \alpha_{mn}}. \quad (5)$$

In our investigation, far-field pattern properties of the OPA are characterized by the array factor, which is determined once  $M$ ,  $N$ ,  $\theta_s$ ,  $\phi_s$ , and the element spacings are specified.

Because of the naturally unequal element distribution, the multi-circular OPA can suppress the grating lobes. However, high-power side lobes still exist in the far-field pattern. To effectively suppress the side lobes, we propose to apply a modified genetic algorithm [16] to search for the ideal element distribution. The genetic algorithm is one of the intelligent approaches, and it has been widely used in engineering design, automatic control, and many other fields thanks to its good characteristics such as simplicity, minimal problem restrictions, and global search capability.

Figure 2 shows the flow chart of the modified genetic algorithm, which consists of initialization, far-field pattern calculation, fitness evaluation, selection, crossover, mutation, and termination. First, a set of initial interelement spacings is generated randomly subject to the limitations of fabrication constraints. They are used as the chromosomes in the modified genetic algorithm. After the far-field pattern calculation, a fitness evaluation is performed to measure how good these chromosomes are at solving the problem. Here, the side lobe suppression ratio is used for the fitness evaluation, which is represented by the PSLL defined by

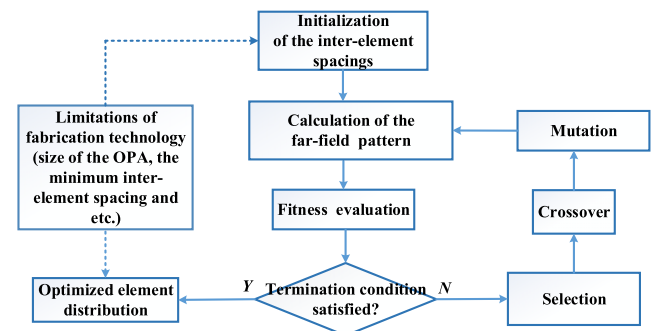


**Fig. 2.** Flow chart of the modified genetic algorithm.

$$\text{PSLL} = \frac{I_{\max \text{ side lobe}}}{I_{\max \text{ lobe}}}, \quad (6)$$

where  $I_{\max \text{ side lobe}}$  is the maximum power of the side lobes, and  $I_{\max \text{ lobe}}$  is the power of the main lobe. In this case, the aim of the modified genetic algorithm is to search for the optimal element distribution to minimize PSLL of the OPA. To do this, a combination of selection, crossover, and mutation is performed to search for the optimal solution by mimicking the same processes that nature uses [16]. The basic idea of this process is to update the chromosomes through crossover and mutation based on selected pieces from the current chromosomes that may contribute to achieving a better fitness evaluation result. Selection is a way of choosing members from the population of chromosomes in a way that is proportional to respective fitness value. Crossover is performed by selecting a random gene along the length of the chromosomes and swapping all the genes after that point. In the mutation, there is a chance that a bit within a chromosome will be flipped to maintain diversity within the population and inhibit premature convergence. This optimization process is repeated until a desired number of cycles, or number of evolutionary generations, has been reached. Validity of the initialization of interelement spacings and the optimized element distribution should be verified with the constraints including the number of phase elements, size of the OPA, and the minimum interelement spacing determined by a state-of-the-art fabrication technique.

It should be noted that, to make sure the optimized OPA is circularly symmetric, only the spacings between adjacent rings are optimized, which are henceforth called radical element spacings of the circular OPA. The phase elements are still uniformly distributed in each ring. In Fig. 1, the spacings between adjacent rings are  $D_1, D_2 - D_1, \dots, D_m - D_{m-1}, \dots, D_M - D_{M-1}$ . In the optimization process, the spacings between adjacent elements are set to be no less than the minimum size ( $d_{\min}$ ) that can be fabricated on an OPA chip. The optimization can be expressed as

$$\begin{cases} \min \text{PSLL} = f(\theta_s, \phi_s, M, N, D_1, D_2, \dots, D_M) \\ \text{s.t. } \min\{\sigma_{\min}, \Delta D_{\min}\} \geq d_{\min}, & D_M < D. \\ \sigma_{\min} = \min\{\sigma_1, \sigma_2, \dots, \sigma_M\} = \sigma_1, \\ \Delta D_{\min} = \min\{D_1, D_2 - D_1, D_3 - D_2, \dots, D_M - D_{M-1}\} \end{cases}, \quad (7)$$

where  $D$  is the size of the OPA chip and  $(\theta_s, \phi_s)$  denotes the direction of the main beam. The fitness function  $f$  in the optimization is defined as the maximum side lobe level within a hemisphere, i.e.,

$$f(\theta_s, \phi_s, M, N, D_1, D_2, \dots, D_M) = \max \left\{ \left| \frac{AF(\theta, \phi)}{AF(\theta_s, \phi_s)} \right| \right\}, \quad (8)$$

where the region of  $(\theta, \phi)$  for which fitness function is valid excluding the direction of main beam  $(\theta_s, \phi_s)$ . Besides,  $\sigma_m$  and  $N$  are related by

$$\sigma_m^2 = 2D_m^2 \left[ 1 - \cos\left(\frac{2\pi}{N}\right) \right]. \quad (9)$$

### 3. SIMULATION AND DISCUSSION

To investigate the performance of the proposed OPA, numerical simulations are performed with MATLAB software. In the simulation, the far-field pattern of the OPA is calculated based on the two-dimensional Fourier transform method [2]. It is essential to select appropriate computing parameters in the modified genetic algorithm, such as the crossover probability, mutation probability, and population size. Until now, there is no theoretical basis for parameter setting, but several recommended settings are proposed [17–19]. Due to the blindness and complexity of parameter selection, the genetic algorithm parameters proposed by De Jong are adopted in this paper. De Jong systematically studies the effect of different parameter combinations on the performance of genetic algorithm. Based on the analyses of five test functions, a set of suggested parameters is applied as follows: population size  $N_{\text{pop}} = 50$ , crossover probability  $P_C = 0.6$ , and mutation rate  $P_m = 0.001$  [17,18]. The iteration number is optimized to be 50, considering the calculation efficiency and optimization performance, and the emitting light wavelength ( $\lambda$ ) is set to  $1 \mu\text{m}$ , which is the commonly used wavelength for the current OPA technique. The multi-circular OPA is composed by 73 ( $M = 6, N = 12$ ) elements. To ensure the minimum interelement spacing is no less than  $1 \mu\text{m}$ , which is determined by the current OPA fabrication technique, the initial value of  $D_1$  is set to be  $2 \mu\text{m}$ . In this case, according to Eq. (9),  $\min\{\sigma_{\min}, \Delta D_{\min}\} = \sigma_1 \geq 1 \mu\text{m}$  is satisfied. In the simulation, the radical element spacings of the multi-circular OPA are kept in the range from 1 and  $3 \mu\text{m}$  (from  $\lambda$  to  $3\lambda$ ).

As a comparison, Fig. 3(a) shows the element distribution of a uniform rectangular  $10 \times 10$  OPA with an element spacing of  $2 \mu\text{m}$ , and the far-field pattern is calculated and shown in Fig. 3(d), where strong grating lobes are clearly observed. In practical applications, these grating lobes would severely restrict the unambiguous scanning range. For a 73-element multi-circular OPA with a fixed radical element spacing of  $2 \mu\text{m}$  shown in Fig. 3(b), the calculated far-field pattern with the main beam direction at  $\theta_s = 0^\circ$  and  $\phi_s = 0^\circ$  is shown in Fig. 3(e), where the grating lobes are eliminated. Meanwhile, bright side lobes are still observed, and the corresponding PSLL is measured to be 0.3686. When the interelement spacings of the circular OPA are optimized through the modified genetic algorithm, distribution of the elements is shown in Fig. 3(c), where the radial element spacings of the optimized multi-circular OPA are 2.000, 1.287, 1.380, 2.105, 2.998, and  $1.048 \mu\text{m}$ , respectively. The far-field pattern with beam forming in direction  $\theta_s = 0^\circ$  and  $\phi_s = 0^\circ$  is shown in Fig. 3(f), and the corresponding PSLL reaches as low as 0.0715. These results indicate that the side lobes can be effectively suppressed by optimizing the OPA with the modified genetic algorithm.

To clearly show the changes during the OPA distribution optimization process, Fig. 4 shows the PSLL values corresponding to different evolutionary generations when performing the modified genetic algorithm, which reflects the convergence process during the optimization. In Fig. 4, the solid curve represents the average level of the PSLL in each evolutionary generation, and the dashed curve is the best PSLL value in each generation. As can be seen, the element distribution of the

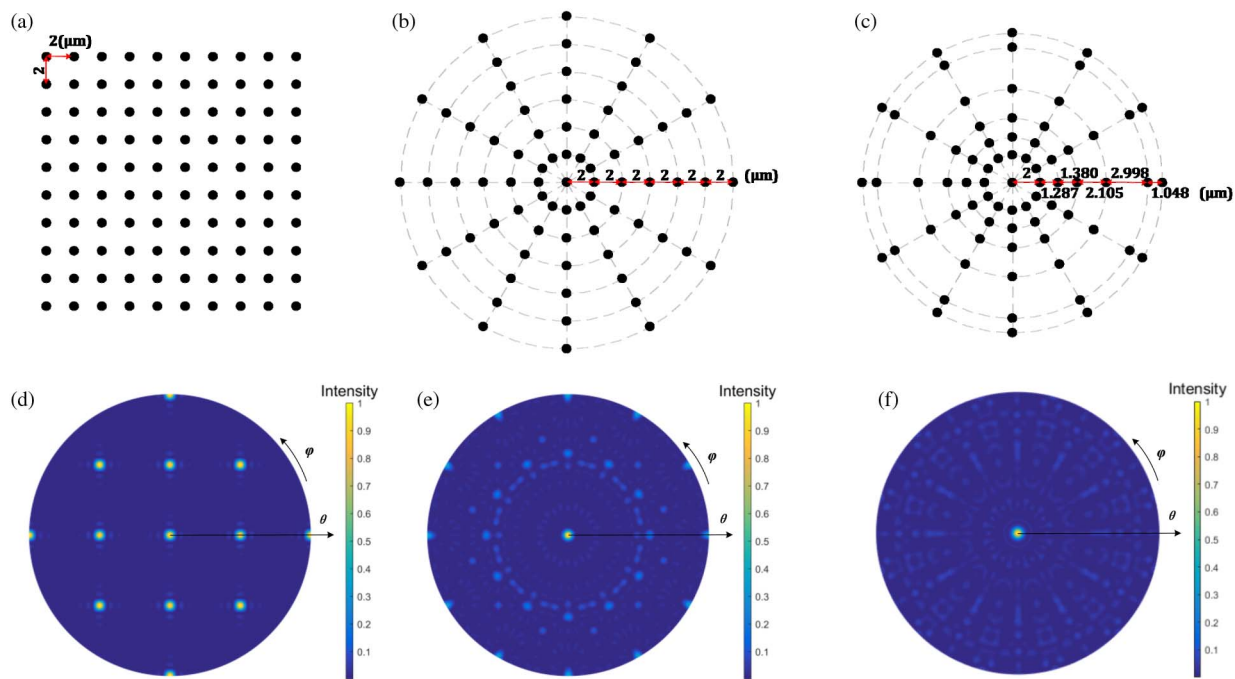


**Fig. 3.** Element distribution and simulated far-field patterns: (a), (b), and (c) are the element distributions of a  $10 \times 10$  uniform rectangular OPA, a uniform circular OPA, and the optimized circular OPA. (d), (e), and (f) are the corresponding simulated far-field patterns.

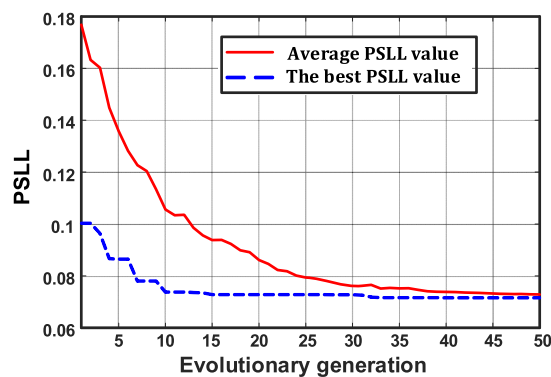


**Fig. 4.** Changes of the average and best PSLL values in each evolutionary generation during the optimization.

**Table 1.** Radical Element Spacings for Several Specific Evolutionary Generations during the Optimization

Generation	Radical Element Spacings ( $\mu\text{m}$ )					
	$D_1$	$D_2 - D_1$	$D_3 - D_2$	$D_4 - D_3$	$D_5 - D_4$	$D_6 - D_5$
1st	2.000	1.878	1.104	2.048	2.998	1.047
10th	2.000	1.275	1.459	2.087	2.998	1.047
20th	2.000	1.312	1.459	2.087	2.998	1.047
30th	2.000	1.312	1.450	2.090	2.998	1.047
40th	2.000	1.287	1.380	2.105	2.998	1.048
50th	2.000	1.287	1.380	2.105	2.998	1.048

multi-circular OPA can be quickly optimized to the ideal distribution through the modified genetic algorithm. For the optimization in achieving the OPA distribution in Fig. 3(c), the best randomly initialized radical element distribution of the OPA is shown in Fig. 5, where the specific radical element spacings are 2.000, 1.878, 1.104, 2.048, 2.998, and 1.047  $\mu\text{m}$ , respectively. The corresponding PSLL is 0.1040. The radical element distributions of the OPA corresponding to the best PSLL values in some specific evolutionary generations are shown in Table 1, which shows the changes of radical element distribution during the optimization process. After optimization, the OPA has the distribution in Fig. 3(c), and the PSLL (0.0715) is greatly reduced compared with that of the initial OPA.

In practice, the optimized PSLL may be affected by the OPA fabrication accuracy. Thus, it is necessary to investigate the side lobe suppression performance with different fabrication accuracies of the proposed multi-circular OPA. According to Ref. [20], the current OPA fabrication by CMOS technology

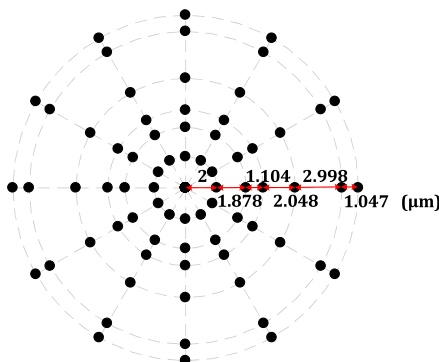


**Fig. 5.** Initialized OPA element distribution when performing optimization by the modified genetic algorithm.



can have an accuracy of from several nanometers to tens of nanometers. Figure 6 shows the possible PSLL values obtained when the element spacing accuracy changes from 5 to 50 nm. This is obtained by multiple simulations in which a random position deviation with a maximum value from 5 to 50 nm is introduced to the OPA elements. In Fig. 6, it is shown that the PSLL of the optimized multi-circular OPA with the modified genetic algorithm can be kept within 0.0715 and 0.090 for a 50 nm fabrication accuracy. With the improvement of fabrication accuracy, the PSLL can further tend to the ideal PSLL, e.g., the PSLL is very close to 0.0715 for a 5 nm fabrication accuracy. These results show that the proposed multi-circular OPA with modified genetic algorithm can allow a certain fabrication deviation.

Since the multi-circular OPA is circularly symmetric, once the OPA is optimized according to a certain elevation direction, the same side lobe suppression can be guaranteed for all the azimuth angles from  $0^\circ$  to  $360^\circ$ . To show this property, the multi-circular OPA distribution is optimized at a beam direction of  $\theta_s = 30^\circ$  and  $\phi_s = 0^\circ$ , applying the modified genetic algorithm. The optimized radial element spacings are 2.000, 1.849, 1.034, 1.203, 1.494, and 1.551  $\mu\text{m}$ , respectively, as shown in Fig. 7, and the optimized PSLL is 0.0852.

With this OPA distribution, the far-field patterns with beam directions at  $(\theta_s, \phi_s)$  of  $(30^\circ, 45^\circ)$ ,  $(30^\circ, 135^\circ)$ ,  $(30^\circ, 225^\circ)$ , and  $(30^\circ, 315^\circ)$  are calculated, as shown in Figs. 8(a)–8(d), respectively.

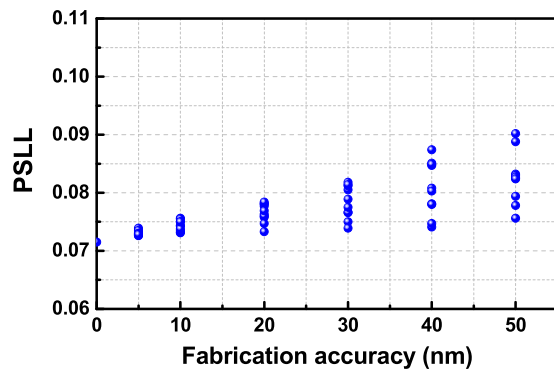


Fig. 6. Relationship between PSLL and different fabrication accuracy.

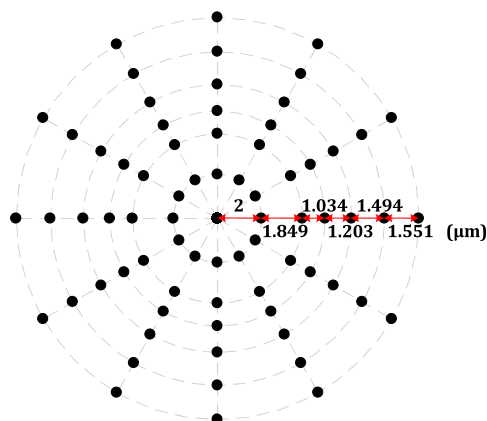


Fig. 7. Optimized OPA element distribution with beam direction  $\theta_s = 30^\circ$  and  $\phi_s = 0^\circ$ .

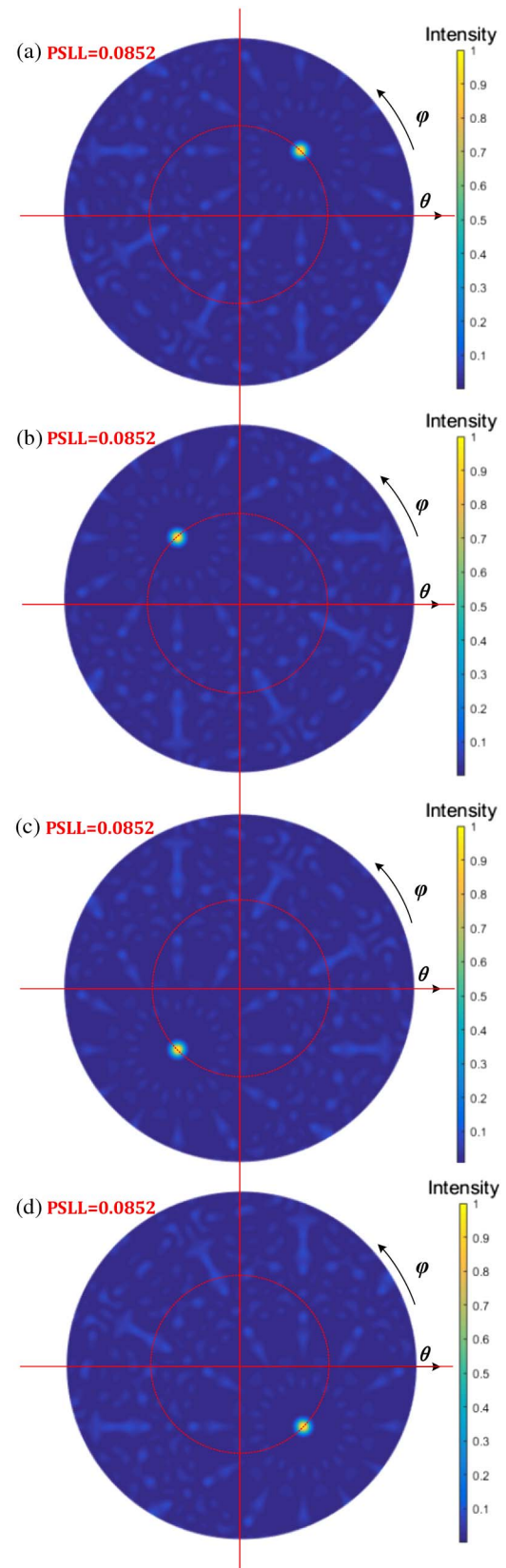


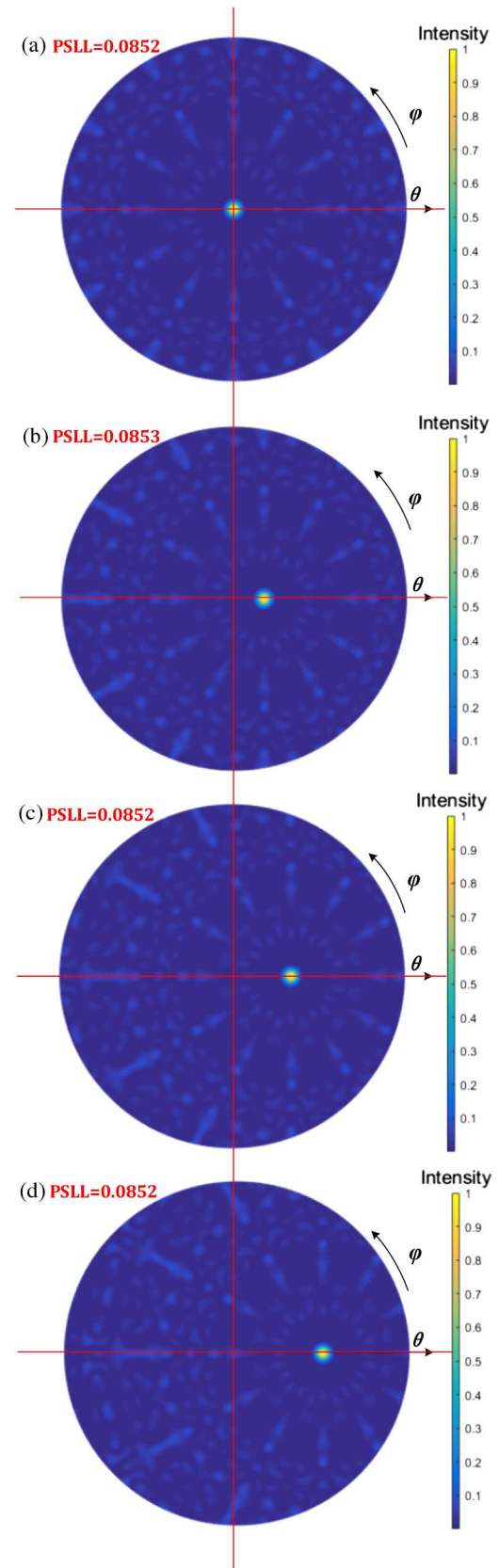
Fig. 8. Simulated far-field patterns of optimized OPA with  $\theta_s = 30^\circ$  and different azimuth directions of (a)  $\phi_s = 45^\circ$ , (b)  $\phi_s = 135^\circ$ , (c)  $\phi_s = 225^\circ$ , and (d)  $\phi_s = 315^\circ$ .

In Fig. 8, the PSLL for different azimuth angles remains 0.0852. This is an obvious advantage of the multi-circular OPA compared with a rectangular OPA, of which the circular asymmetry would make the PSLL not a constant for different azimuth angles.

Another advantage of the proposed multi-circular OPA is that when the OPA distribution is optimized at a certain elevation direction of  $\theta_s$ , the PSLL for beam directions with an elevation angle smaller than  $\theta_s$  would change very slightly. Based on the optimized OPA with a beam direction at  $\theta_s = 30^\circ$  and  $\phi_s = 0^\circ$  (see Fig. 7), the far-field patterns when  $\theta_s$  changes to  $0^\circ$ ,  $10^\circ$ ,  $20^\circ$ , and  $30^\circ$  are calculated while the azimuth angle is kept at  $0^\circ$ . The results are shown in Figs. 9(a)–9(d), respectively. The corresponding PSLL is 0.0852, 0.0853, 0.0852, and 0.0852, respectively, which is nearly unchanged. If the elevation direction exceeds  $30^\circ$ , the PSLL would get worse obviously. For example, the PSLL corresponding to the elevation angle of  $32^\circ$ ,  $45^\circ$ , and  $60^\circ$  is increased to 0.1095, 0.1184, and 0.1203, respectively.

The previous results show that, for a given elevation direction  $\theta_s$ , the optimized OPA distribution is suitable for optical beam steering with an elevation angle no more than  $\theta_s$ , without considering the azimuth direction. To further verify this property, PSLL of the multi-circular OPA optimized for beam direction at  $\theta_s = 30^\circ$  and  $\phi_s = 0^\circ$  is investigated when the elevation and azimuth change with a small step. Table 2 shows the simulated PSLL values when  $\theta_s$  is  $0^\circ$ ,  $5^\circ$ ,  $10^\circ$ ,  $15^\circ$ ,  $20^\circ$ ,  $25^\circ$ , and  $30^\circ$ , and  $\phi_s$  is  $0^\circ$ ,  $45^\circ$ ,  $90^\circ$ ,  $135^\circ$ ,  $180^\circ$ ,  $225^\circ$ , and  $315^\circ$ . Through the result, it is found that the PSLL variation is kept within 0.001 through the whole scanning range with  $\theta_s \leq 30^\circ$ . This property indicates that once the multi-circular OPA is optimized towards a specific direction by the modified genetic algorithm, a wide-angle optical beam steering can be guaranteed without updating the OPA distribution, which is highly desired to achieve fast beam steering.

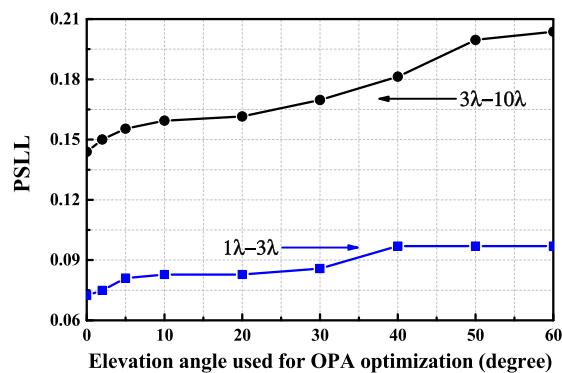
Finally, it is necessary to investigate the PSLL when the proposed multi-circular OPA is optimized towards different elevation directions. Because the elevation direction used for OPA optimization determines the optical beam scanning range, choosing the best side lobe suppression according to the required scanning range can help to improve the performance of the OPA. Through extensive simulations, the optimized PSLL when the OPA is optimized at different elevation angles is obtained, as shown in Fig. 10. Here, the results when the element spacings are kept within the ranges of  $1\lambda - 3\lambda$  and  $3\lambda - 10\lambda$  are investigated, respectively. The blue curve with square dot in Fig. 10 shows the relationship between the PSLL and elevation angle used for OPA optimization when the element spacing is kept within  $1\lambda - 3\lambda$ . As can be seen, when the elevation angle used for OPA optimization increases from  $0^\circ$  to  $40^\circ$ , the PSLL becomes larger from 0.072 to 0.096. This result means there is a tradeoff between a lower PSLL and a larger beam steering range, i.e., the side lobe suppression becomes worse when a large beam scanning range is required in the elevation direction from  $0^\circ$  to  $40^\circ$ . When the elevation angle used for OPA optimization exceeds  $40^\circ$ , the PSLL of the optimized OPA tends to be invariable at 0.096. When the element spacing is allowed in a larger range of  $3\lambda - 10\lambda$ , a similar trend is observed as the elevation angle used for optimization increases,



**Fig. 9.** Simulated far-field patterns of optimized OPA with  $\phi_s = 0^\circ$  and different elevation directions of (a)  $\theta_s = 0^\circ$ , (b)  $\theta_s = 10^\circ$ , (c)  $\theta_s = 20^\circ$ , and (d)  $\theta_s = 30^\circ$ .

**Table 2. PSLL of Optimized Multi-circular OPA in a Wide Two-Dimensional Scanning Range**

$\phi$	$\theta$						
	0°	5°	10°	15°	20°	25°	30°
0°	0.0852	0.0851	0.0853	0.0852	0.0852	0.0851	0.0852
45°	0.0852	0.0852	0.0853	0.0853	0.0855	0.0855	0.0857
90°	0.0852	0.0851	0.0853	0.0852	0.0852	0.0851	0.0852
135°	0.0852	0.0852	0.0853	0.0853	0.0855	0.0855	0.0857
180°	0.0852	0.0851	0.0853	0.0852	0.0852	0.0851	0.0852
225°	0.0852	0.0852	0.0853	0.0853	0.0855	0.0855	0.0857
270°	0.0852	0.0851	0.0852	0.0852	0.0852	0.0851	0.0852
315°	0.0852	0.0852	0.0853	0.0853	0.0855	0.0855	0.0857

**Fig. 10.** Relationship between optimized PSLL and the elevation angle used for OPA optimization when the element spacing is kept within  $1\lambda - 3\lambda$  and  $3\lambda - 10\lambda$ , respectively.

as shown by the block with circular dots in Fig. 10. However, the achieved PSLL is deteriorated compared with the case for element spacing kept within  $\lambda - 3\lambda$ . Specifically, for a beam steering direction of 0°, the optimized PSLL is 0.144, and the PSLL exceeds 0.2 when the beam steering range reaches 60°.

In the previous demonstration, a 73-element OPA is adopted. It should be noted that the proposed multi-circular OPA distribution and its optimization method is still suitable when the element number changes. Numerical simulation results can confirm that similar properties can be achieved by the multi-circular OPAs with different element numbers, which means the proposed multi-circular OPA is a good solution to realize fast and wide-range beam steering with good side lobe suppression. In this work, multi-circular OPAs with ideal point radiators and uniform amplitude excitation are adopted. In practice, choosing a proper radiating element's diffraction envelope could further suppress the side lobe and improve power efficiency [21]. Besides, to improve the side lobe suppression capability, a combination of both amplitude and phase control of the OPA element can be applied [22].

#### 4. CONCLUSIONS

We have proposed a fast and wide-range optical beam steering method applying an optimized multi-circular OPA. By optimizing the radial element spacings of the multi-circular OPA, the side lobes can be well suppressed. Performance of

the proposed OPA is investigated through numerical simulations. The simulation results show that when the OPA is optimized towards a specific elevation direction, a wide-angle optical beam steering with nearly the same PSLL can be achieved without updating the OPA distribution. Therefore, it is capable to implement fast and wide-range optical beam scanning. Besides, the relationship between the optimized PSLL and the elevation angle used for OPA optimization is also investigated, which is helpful in achieving the best side lobe suppression. The proposed multi-circular OPA may find good applications in laser radar, high-resolution display, and free space optical communications.

**Funding.** National Natural Science Foundation of China (NSFC) (61527820); Fundamental Research Funds for Central Universities (NS2018028).

#### REFERENCES

1. J. Montoya, A. Sanchez-Rubio, R. Hatch, and H. Payson, "Optical phased-array lidar," *Appl. Opt.* **53**, 7551–7555 (2014).
2. J. Sun, E. Timurdogan, A. Yaacobi, E. S. Hosseini, and M. R. Watts, "Large-scale nanophotonic phased array," *Nature* **493**, 195–199 (2013).
3. R. Fatemi, B. Abiri, and A. Hajimiri, "An  $8 \times 8$  heterodyne lens-less OPA camera," in *Conference on Lasers and Electro-Optics 2017*, San Jose, California USA (Optical Society of America, 2017), p. JW2A.9.
4. A. B. Meinel and M. P. Meinel, "Optical phased array configuration for an extremely large telescope," *Appl. Opt.* **43**, 601–607 (2004).
5. A. Linnenberger, S. Serati, and J. Stockley, "Advances in optical phased array technology," *Proc. SPIE* **6304**, 63040T (2006).
6. A. Polishuk and S. Arnon, "Communication performance analysis of microsatellites using an optical phased array antenna," *Opt. Eng.* **42**, 2015–2024 (2003).
7. J. L. Pita, I. Aldaya, O. J. S. Santana, L. E. E. de Araujo, P. Dainese, and L. H. Gabrielli, "Side-lobe level reduction in bio-inspired optical phased-array antennas," *Opt. Express* **25**, 30105–30114 (2017).
8. C. Zhao, C. Peng, and W. Hu, "Blueprint for large-scale silicon optical phased array using electro-optical micro-ring pixels," *Sci. Rep.* **7**, 17727 (2017).
9. W. S. Rabinovich, P. G. Goetz, M. W. Pruessner, R. Mahon, M. S. Ferraro, D. Park, E. F. Fleet, and M. J. DePrenger, "Two-dimensional beam steering using a thermo-optic silicon photonic optical phased array," *Opt. Eng.* **55**, 111603 (2016).
10. Y. Wang and M. C. Wu, "Micromirror based optical phased array for wide-angle beamsteering," in *International Conference on MICRO Electro Mechanical Systems*, Las Vegas, Nevada, USA (IEEE, 2017), pp. 897–900.
11. D. Kwong, A. Hosseini, Y. Zhang, and R. T. Chen, "1 × 12 unequally spaced waveguide array for actively tuned optical phased array on a silicon nanomembrane," *Appl. Phys. Lett.* **99**, 051104 (2011).
12. T. Komljenovic, R. Helkey, L. Coldren, and J. E. Bowers, "Sparse aperiodic arrays for optical beam forming and LIDAR," *Opt. Express* **25**, 2511–2528 (2017).
13. S. Yin, J. H. Kim, F. Wu, P. Ruffin, and C. Luo, "Ultra-fast speed, low grating lobe optical beam steering using unequally spaced phased array technique," *Opt. Commun.* **270**, 41–46 (2007).
14. D. Zhang, F. Zhang, and S. Pan, "Grating-lobe-suppressed optical phased array with optimized element distribution," *Opt. Commun.* **419**, 47–52 (2018).
15. P. Ioannides and C. A. Balanis, "Uniform circular and rectangular arrays for adaptive beamforming applications," *IEEE Antennas Wireless Propag. Lett.* **4**, 351–354 (2005).
16. J. H. Holland, *Adaptation in Natural and Artificial Systems* (University of Michigan, 1975).
17. K. A. De Jong, *An Analysis of the Behavior of a Class of Genetic Adaptive Systems* (University of Michigan, 1975).

18. K. A. De Jong and W. M. Spears, "An analysis of the interacting roles of population size and crossover in genetic algorithms," in *Proceedings of the First Workshop Parallel Problem Solving from Nature*, Heidelberg, Germany (Springer-Verlag, 1990), pp. 38–47.
19. J. J. Grefenstette, "Optimization of control parameters for genetic algorithms," *IEEE Trans. Syst., Man, Cybern.* **16**, 122–128 (1986).
20. S. K. Selvaraja, W. Bogaerts, P. Dumon, D. V. Thourhout, and R. Baets, "Subnanometer linewidth uniformity in silicon nanophotonic waveguide devices using CMOS fabrication technology," *IEEE J. Sel. Top. Quantum Electron.* **16**, 316–324 (2010).
21. D. D. Macik, T. E. Bravo, S. M. Pentecost, F. A. Espinal, and C. K. Madsen, "Optimization of electro-optic phase shifters for integrated optical phased arrays," *Proc. SPIE* **10181**, 1018105 (2017).
22. Y. Jin, A. Yan, Z. Hu, Z. Zhao, and W. Shi, "High speed and low side lobe optical phased array steering by phase correction technique," *Proc. SPIE* **8847**, 884716 (2013).